DESIGN, ANALYSIS AND TESTING OF A POSTBUCKLING CO-CURED COMPOSITE CONTROL SURFACE

Murray L. Scott[1], Alan K.H. Cheung[2], Paul D. Newman[3]

Cooperative Research Centre for Aerospace Structures Limited
506 Lorimer Street, Fishermens Bend, Victoria, 3207, Australia

Abstract

The design, analysis and testing of a postbuckling co-cured advanced carbon fibre composite control surface is presented in this paper. The structure investigated represents a typical control surface on a medium size jet transport aircraft wing. With an original sandwich construction as the baseline design, the primary objectives for the new composite control surface were to reduce weight and manufacturing cost, and to achieve or exceed the existing requirements for quality, durability and damage tolerance. The use of carbon fibre composites ensured excellent fatigue and corrosion properties, and the avoidance of honeycomb sandwich construction greatly improved damage tolerance. In order to achieve significant weight savings over the baseline, emphasis was placed on a thin-skinned postbuckling design. Co-curing the aft box structure eliminated the use of many fasteners and pad-ups, which reduced weight and cost.

Geometric nonlinear finite element analyses have been successfully conducted, showing MSC/NASTRAN to be an appropriate tool for analysing complex postbuckling structures. Full scale tests showed no damage after the design ultimate load was achieved and also that buckling occurred in the top and bottom skins of the control surface. The buckling mode shapes and strain characteristics agreed well with analyses. A weight saving for the control surface aft box structure of 34% was achieved. It is concluded that this postbuckling composite control surface design shows tremendous potential as a more efficient alternative for the next generation of transport aircraft.

Introduction

Stiffened panels in semi-monocoque construction have been extensively employed in metallic aerospace structures for many years. Incorporating postbuckling design concepts into such structures has further optimised their structural performance. However, the progressive introduction of advanced carbon fibre composites into aerospace structures presents new challenges in the design and manufacture of these components. Carbon fibre reinforced composites in honeycomb sandwich panels have now been widely used in control surfaces for commercial transport aircraft for well over a decade. Typical design configurations for components, such as ailerons, incorporate carbon fibre/epoxy ribs and spars, which are mechanically fastened to honeycomb sandwich skins. Poor impact resistance, water ingression, skin/core delamination and costly repair of damaged skins are the most common causes of problems raised by operators of aircraft with this type of construction.

In recent years the imperative to reduce the cost of manufacturing advanced fibre composite components and wherever possible improve their operational performance has led to innovative design concepts being proposed, which do not rely on honeycomb sandwich construction techniques [1-2]. The most promising concept for the relatively lightly loaded components found in control surface structures is that characterised by thin integrally stiffened composite skins, which buckle below limit load levels in a similar manner to their metallic counterparts.

The design and manufacturing technologies associated with composite honeycomb sandwich panels were considered the baseline for the new composite control surface design presented in this paper. The structure investigated represents a typical control surface on a medium size jet transport aircraft. In order to demonstrate the weight and cost saving potential of thin buckling skins with integral blade-stiffening, a complete control surface has been designed which incorporates many innovative features. Central to this task was the selection of a one-piece composite manufacturing process which

[1] Department of Aerospace Engineering, Royal Melbourne Institute of Technology.
[2] Cooperative Research Centre for Aerospace Structures Limited.
[3] Rockwell ASTA Components.

enabled the blade-stiffened skin, rear spar and ribs to be co-cured.

Design

Objectives

The objectives for the new design were as follows : to reduce the mass of the control surface aft box structure by 30%; to achieve or exceed existing requirements for quality, durability and damage tolerance; and to achieve existing requirements for environmental degradation and stiffness criteria.

Design Configuration

The overall dimensions of the control surface are 2.8 m × 0.4 m, with a local sweep angle of 16 degrees. The control surface is supported by four hinges at the front spar. A 1.7 m long balance tab is located at the trailing edge extending from the inboard end of the structure. The control surface is actuated by a single control rod next to the inboard hinge. The baseline honeycomb structure has been redesigned by using thin buckling skins incorporating co-cured multi-blade-stiffeners [3]. There is a total of nine ribs and twelve stiffeners, which are positioned chordwise along the span, as shown in Figure 1.

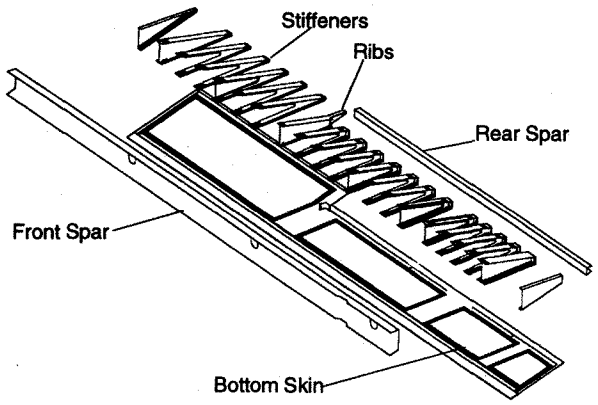

FIGURE 1 - Configuration of the Control Surface (Top Surface Not Shown)

Design Features

To achieve significant weight savings over the honeycomb sandwich baseline structure, emphasis was placed on a thin-skinned postbuckling design. Buckling was only permitted in the skins of the box structure. Front and rear spars, which carry the bending loads on the control surface, were designed not to buckle prior to design ultimate load. Some sections of the upper and lower skins however, were reinforced to prevent buckling. This was necessary to allow attachment of a fairing to the lower skin for the tab control rods, and skin strengthening at the critical areas. Multiple chordwise blade-stiffeners were incorporated to stiffen the thin buckling skin.

The aft box structure of the control surface, which includes the upper and lower skins, blade-stiffeners, rear spar and internal ribs, were all co-cured. This eliminated the use of many fasteners and pad-ups, and reduced weight and cost. The closure ribs and front spar were mechanically fastened to the box structure. This manufacturing method allowed forward removal of the tooling [4].

Matching the stiffness of the baseline sandwich construction control surface was required. Since similar front and rear spars to the baseline control surface were used, bending stiffness has essentially not been changed. Matching the torsional stiffness of the baseline control surface required a multi-rib structural design with the thin skins supported by multiple blade-stiffeners, as shown in Figure 2. The skin consists of two pairs of ±45° plies to resist the torsional loading and two 0° (spanwise plies) and one 90° (chordwise plies) to transfer the air loading to the surrounding structure. There are also local skin build-ups at the front and rear spars and around major hinge ribs.

FIGURE 2 - Typical Skin-Stiffener Interface

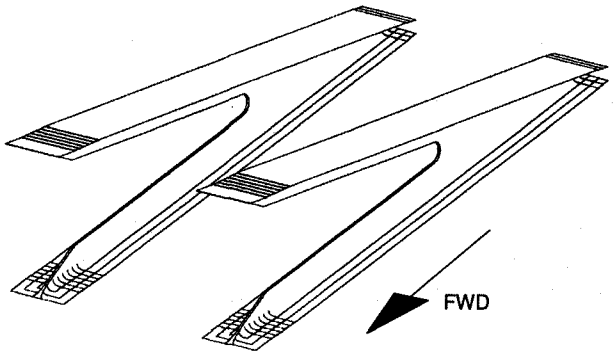

FIGURE 3 - Typical Outboard Stiffeners

The blade-stiffeners had to be terminated or "run-out" at the front spar which required careful design to prevent stiffener disbonding. Local skin ply build-ups were used to inhibit skin buckling at the stiffener run-outs. All stiffening members were double flanged and blade "softening" or local blade ply "drop-offs" were incorporated to prevent buckling at the skin interface and to reduce peel stresses. At the trailing edge and rear spar locations, the upper and lower surface blade-stiffeners join together forming a "semi-rib" which avoids stiffener run-outs and improves torsional stiffness, as shown in Figure 3.

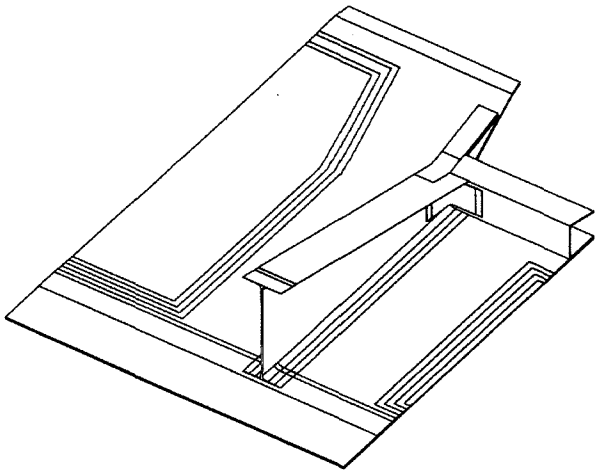

FIGURE 4 - The "Kink Rib" (Top Skin and Front Spar Not Shown)

The ribs were typically made from the similar web-skin interface as the stiffener, with two "C"-sections combined back-to-back forming an "I"-section. The inboard ribs were connected to the rear spar by wrapping the rib web towards the rear spar web to form a pair of rib flanges. The two closure ribs were mechanically fastened to the structure, as was the front spar. Special attention was focussed on the design of the "Kink Rib", which is located outboard of the rear spar termination. A shear-tie between the web of the rib and the web of the rear spar improves stiffness and load transfer. Doublers were added to the flanges of the rib at the kink joint in order to locally improve strength. Additional skin ply build-ups were incorporated to prevent buckling of the skin near the trailing edge of the Kink Rib, as shown in Figure 4.

Computer Aided Design/Manufacture Model

CATIA was the computer aided design and manufacturing environment chosen for the project due to its extensive use in the aerospace industry. The CATIA design database was used as the sole design authority and was transferred digitally between the design centre in Melbourne and the manufacturing centre in Sydney.

A valuable feature is the Boolean capabilities of the CATIA solids. This algebraic management of solids allows the user to perform intersections, subtractions and additions. This technique was applied in the resulting geometry of the ribs, stiffeners and skins for each one of the control surface bays. The resulting solid is then the 3-D model of the tool mandrel to be used for manufacturing, as shown in Figure 5.

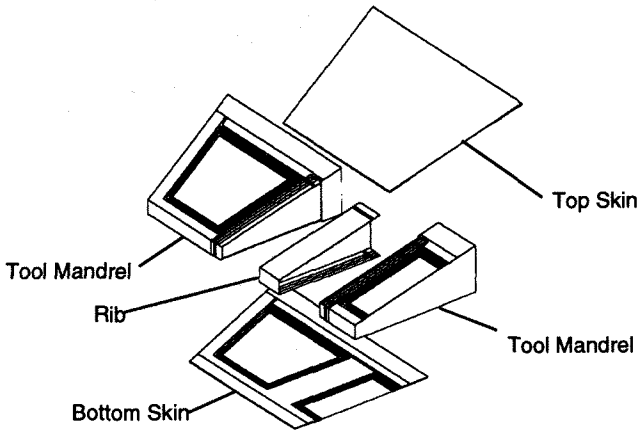

FIGURE 5 - Tool Mandrels Created by CATIA Boolean Operations

Analysis

Loading Conditions

In this study, two load cases were considered. The external loads were obtained as an extrapolation from the "11.2° Down" condition of a typical mid-size jet transport aircraft. A 2-D chordwise airload distribution was obtained which was distributed constantly along the span. In the finite element model, follower vector loads were applied to the top and bottom skins.

The second load case is the induced loading due to sympathetic bending of the wing. Enforced displacements were applied vertically downwards at the middle two hinges to simulate the radius of curvature induced by such wing bending. The critical load case is considered to be the combination of the above two cases.

Finite Element Model

The finite element (FE) model of the control surface was constructed using the pre- and post-processor P3/PATRAN (see Figure 6). The model contains 14,000 four-noded quadrilateral elements and a total of 70,000 degrees of freedom. A 2-D orthotropic material model consistent with classical laminate theory was used.

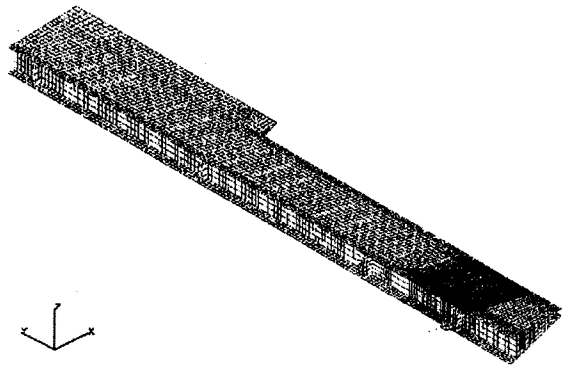

FIGURE 6 - The Finite Element (FE) Model

In order to reduce the size of the model, blade-stiffeners were modelled using 2-D bar elements, as shown in Figure 7, where appropriate laminate properties were calculated and applied to the off-set bar elements. At the region where the stiffeners joined to form a "semi-rib" near the trailing edge and rear spar, shell elements were used. A minimum of six elements between stiffeners was used to effectively represent the half waves of the buckling skin. The control rod was fixed in all six degrees of freedom at the wing end, and the control surface was constrained to rotate about the hinge line.

Detail Region

A refined mesh was used to model the critically loaded region near the actuator rod hinge. Blade-stiffeners were accurately modelled using shell elements allowing more detail to be included, enabling the stiffener run-out and ply build-ups/drop-offs to be incorporated. Modelling of the stiffeners correctly using shell elements, required at least four rows of elements along the height of the stiffener; otherwise, an artificially high stiffness will occur in the FE model for the stiffener [5]. The individual ply build-ups in the skin were also modelled for more accuracy, as was the actuator rod hinge including individual fasteners to provide a realistic load transfer from the control surface box structure.

Finite Element Analysis

The FE analysis package MSC/NASTRAN was used to perform the complex buckling analysis of the control surface structure. Linear buckling analysis using the Lanczos method in MSC/NASTRAN

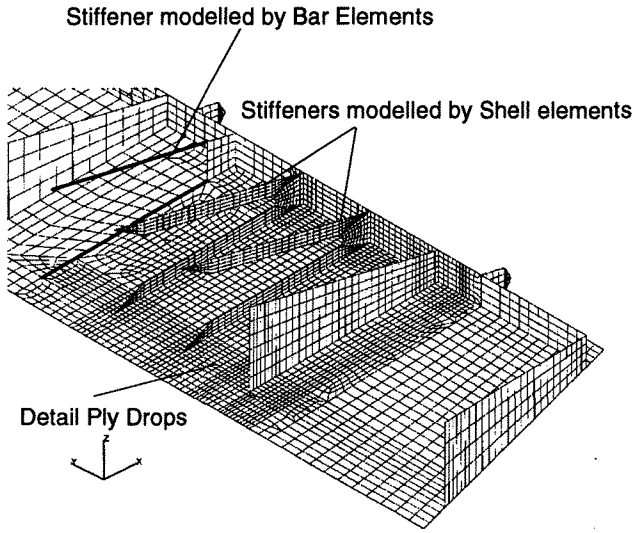

FIGURE 7 - Detail Region of the FE Model (Front Spar and Top Skin Not Shown)

performs an eigensolution to predict the eigenvalues and eigenvectors, where buckling loads and their mode shapes can be determined. This enables the point of buckling to be defined and hence the buckling ratio (the ratio of ultimate load to buckling load) to be determined.

Geometric nonlinear analysis using the Modified Newton-Raphson method [6] was performed. The load was incremented by ten equal load steps and the stiffness matrix was updated automatically by MSC/NASTRAN. At each load step, an iterative method was used to derive the correct solution.

Analysis Results

The results presented are for the critical load case, which includes the enforced displacements for induced bending and the 2-D chordwise airload distribution. A linear static analysis of the control surface was conducted. Large out-of-plane deflections were encountered in the skins due to buckling and pressure loads. Since small deflections are assumed in linear analysis, membrane stiffening effects are not considered. The out-of-plane deflections are higher and the predicted stress levels are lower, hence the margins of safety are not conservative.

A linear buckling solution was also performed, where the computational run time was 1.7 hours. The first nine modes of buckling occurred at the outboard region due to its larger unsupported skin and wider stiffener pitch.

Finally, a geometric nonlinear analysis was performed. This analysis required 5.0 hours of computational run time to complete. The maximum deflection was 44 mm at the outboard tip, as shown in Figure 8. Complex compression/shear buckling of the top skin can be seen.

The deflections on the control surface versus the load for both linear and nonlinear analyses are shown in Figure 9. It should be noted that this graph is not end shortening versus load as is typical with results of nonlinear analyses. The tip deflection of the control surface is a function of the torsional stiffness of the structure and the bending stiffness of the ribs, stiffeners and rear spar. Up to the point of buckling, the tip deflection is the same for linear and nonlinear analyses. After the first buckling of the skins, the stiffness of the box structure changes, hence the difference in the linear and nonlinear analysis curves. The nonlinear load factor versus tip deflection curve indicates that the box structure increases in torsional stiffness after buckling, resulting in reduced tip deflections for a given load. A complex interaction of compression and shear buckling, combined with skin air-pressure loads occurs.

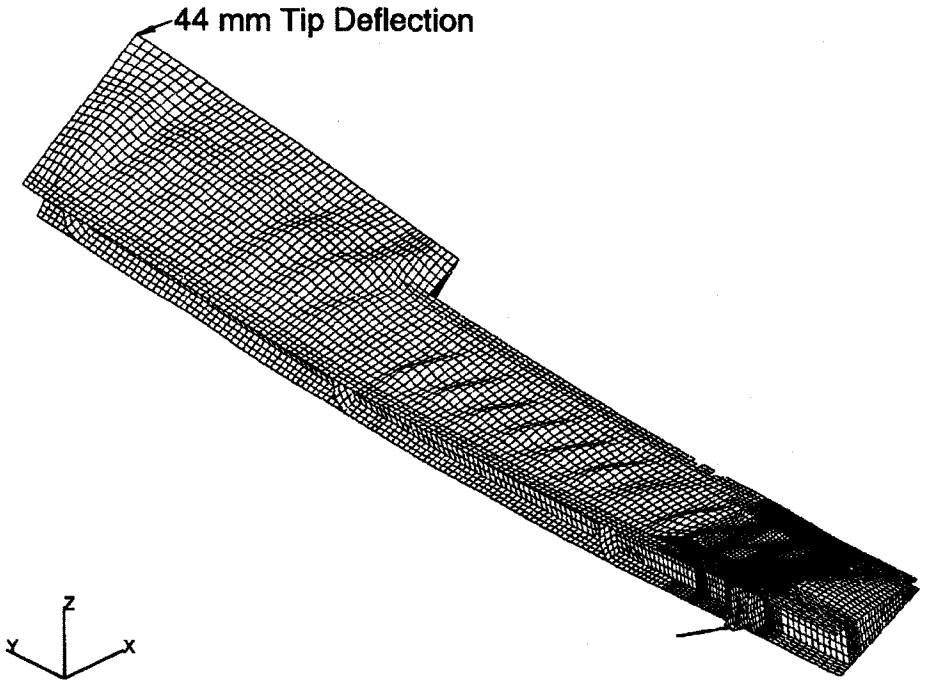

FIGURE 8 - Deformed Plot from Nonlinear Analysis

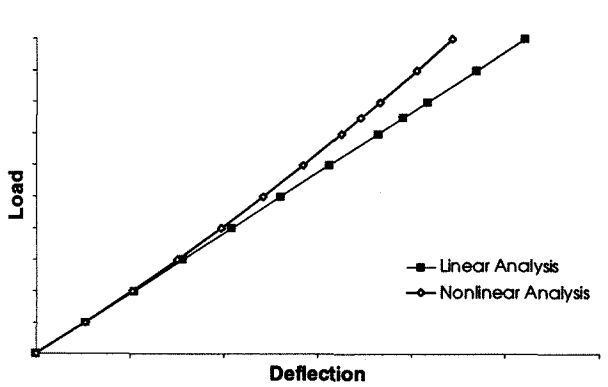

FIGURE 9 - Comparison Between Linear and Nonlinear Analyses

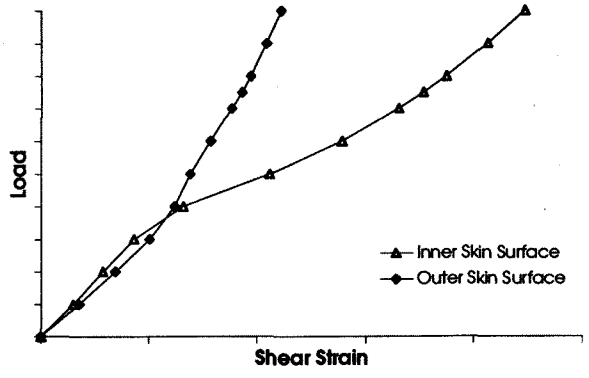

FIGURE 10 - Load/Shear-Strain Plot of Critical Element in the Top Skin

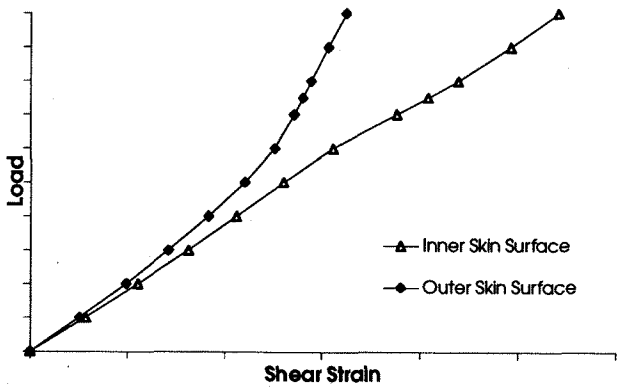

FIGURE 11 - Load/Shear-Strain Plot of Critical Element in the Bottom Skin

Diagonal type shear buckling of the upper skin between stiffeners and ribs was observed in analytical results. Surface strain plots of critical elements at the top and bottom skins are shown in Figures 10 and 11; the results are extracted for the in-board skins near the actuator rib.

At load levels before buckling began, the outer surface of the top skin exhibited a higher strain than the inner surface under the same load factor (see Figure 10). This behaviour is due to the fact that load was applied by pressure in the direction towards the outer skin surface. However, at load levels after buckling, the buckling strain started to take over and the situation reversed. Similar behaviour is observed for the bottom skin (see Figure 11). However, since the pressure load was applied towards the inner surface, the inner skin surface constantly showed a higher strain when compared to the outer skin surface.

Testing

In order to assess the performance of the structure and validate the analysis, a full scale static test program was conducted with the aim of measuring strains and displacements and observing buckling behaviour as load was applied. The test rig was designed to enable testing with and without the wing bending displacement applied so that the critical case could be approached from less severe load cases. Tests were carried out at room temperature and the test article was dry.

Test Set-up

The stiffened skin structure was permitted to buckle freely by applying load via contour boards to the ribs. This was thought to be more desirable than directly loading the thin-skins via pressure pads. The latter method involves the risk of damaging the skins and requires a more complex loading system.

The arrangement used was the application of load to each of the nine ribs using six electro-mechanical actuators driven by a closed loop control system. Load levels are specified in customised software written for the system, and the load for each actuator and the ramp rate can be varied with ease.

As one of the main interests in the testing was the buckling behaviour of the structure, the control surface was mounted in the rig with its chord in the vertical plane. This enabled excellent viewing of the top and bottom skins as load was applied, but necessitated the application of loads in the horizontal plane, as shown in Figure 12.

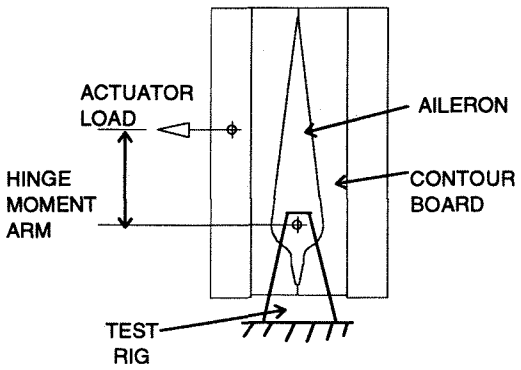

FIGURE 12 - Test Set-up Schematic

The wing bending displacements were applied at the middle two hinges; these displacements being normal to the chord. To enable testing with and without the wing bending displacements applied, these two hinge fittings on the test rig were made adjustable in the normal-to-chord direction. A load cell was also incorporated into each of these fittings to measure normal-to-chord hinge loads.

Instrumentation

Instrumentation for the tests consisted of 52 strain gauge channels, which were mainly back-to-back electrical resistance strain gauge rosettes on the top and bottom skins. The Actuator Rib was also instrumented with a rosette, and linear gauges were placed on the selected stiffeners. The strain gauges on the skins were located at the areas of expected maximum strains and critical buckling areas based on the finite element analysis results.

Three Linear Variable Displacement Transducers (LVDT) were placed along the trailing edge at the inboard end, at the end of the tab region and on the outboard tip. Two additional LVDTs were placed normal to the skin, mounted on the nearest contour board, to measure skin out-of-plane displacements. These were placed near the Kink Rib (where the balance tab ends) and near the Actuator Rib. The control rod was instrumented to enable monitoring of the applied hinge moment during the tests, having previously been calibrated.

At two locations, moiré grid panels were placed over the bottom skin to enhance the buckling images, however no quantitative analysis of the buckling was carried out using these panels. The locations selected were immediately outboard of the balance tab, where buckling was expected to commence, and adjacent to the Actuator Rib where the highest strains were predicted. Photographs of each panel were taken at each load increment and video cameras recorded each test, showing top and bottom skins.

All instrumentation was connected to a data acquisition system to enable the rapid sampling of all load, displacement and strain channels.

Loading

To simulate the air load case, the distributed pressure loading was resolved to each rib. The aerodynamic balance tab was not present on the test article, and the loads applied by the tab were similarly resolved to the nearest ribs.

The chordwise location of each rib load was chosen to approximate the spanwise hinge moment distribution. After adjustment of individual rib loads and moment arms, a loading system which satisfactorily represented the airload distribution and hinge moment distribution was achieved. The middle two hinges were displaced 9.9 mm and 7.5 mm respectively to simulate the wing bending displacements.

Loads were first applied to limit level, without and then with wing bending, and then to ultimate level, without and then with wing bending. This ensured the tests were carried out from the least severe load case to the most severe load case.

Results

The aileron survived the design ultimate load, including the wing bending displacements, without any form of failure and non-destructive testing showed no damage to the structure internally.

Due to the deflection of the aileron under load, particularly at the outboard end, the relationship between rib loads and hinge moment for the tests was non linear. This problem is made worse by the fact that most of the airload and hinge moment are developed at the outboard region of the aileron where deflections are large compared to the inboard region. The moment arms were chosen such that the design ultimate hinge moment occurred at the design ultimate rib loads.

As the deflection of the structure is mainly dependent on the torque applied, the measured displacements are shown in Figure 13, plotted against load factor based on hinge moment.

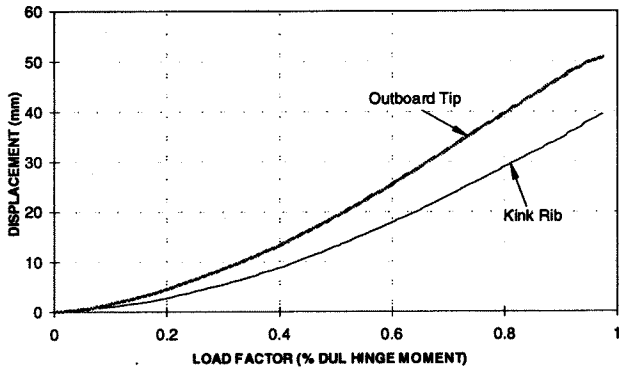

FIGURE 13 - Displacement at the Trailing Edge

The figure shows the displacements of the trailing edge middle and outboard LVDTs relative to the inboard LVDT, and so in essence illustrates the amount of twist of the structure under load. As the spanwise torque distribution is really only at the design distribution at ultimate load, the shape of the curve can only be loosely interpreted. Nevertheless, the final displacement at the ultimate load of approximately 50 mm agrees quite well with the analytical model.

As predicted, examination of the shear strain results showed the stress field to be dominated by shear. Peak strains were at locations close to the Actuator Rib (see Figures 14 and 15). The initial strains are caused by the wing bending displacements which were sufficient to buckle the top skin panels mid-span.

Both figures show distinct buckling trends as anticipated, indicated by the diverging plots of inner and outer rosettes, with the top skin plot showing a change in buckling mode at 90% DUL and a corresponding sudden increase in strain level. Figure

16, showing the shear strain on the bottom skin close to Rib 3, illustrates a typical transition to the buckled state at approximately 70% DUL.

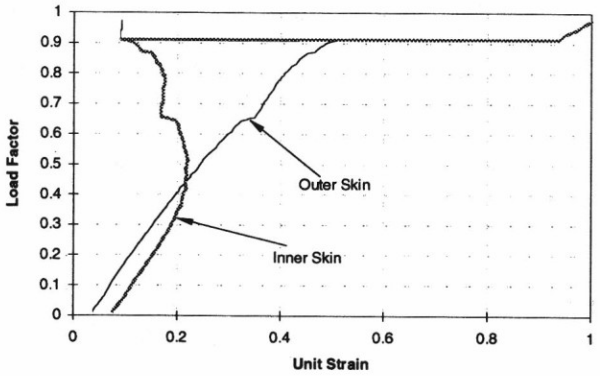

FIGURE 14 - Top Skin Shear Strains Near Actuator Rib

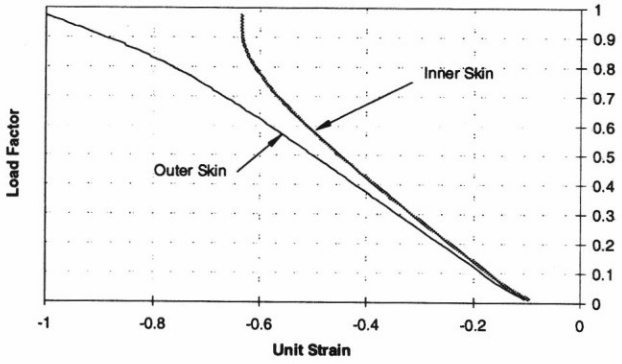

FIGURE 15 - Bottom Skin Shear Strains Near Actuator Rib

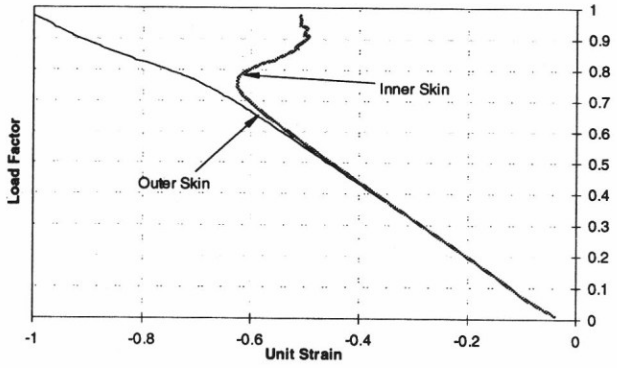

FIGURE 16 - Bottom Skin Shear Strain - Inboard Region

Figure 17 shows the shear strain in the outboard region adjacent to the Kink Rib where the balance tab ends. The strain here was considerably less than the inboard region. The plot shows a large increase in shear strain where the buckling mode shape changed at around 42% DUL and the load/strain relationship is highly nonlinear after this mode change.

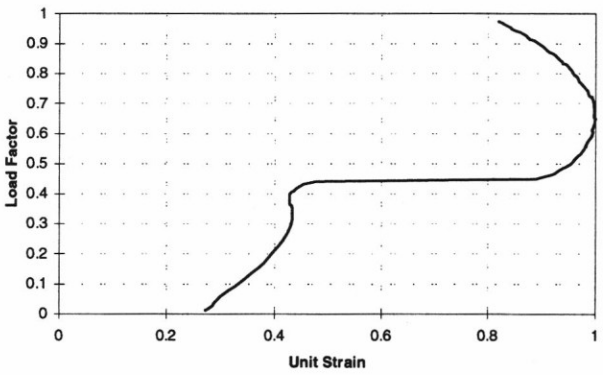

FIGURE 17 - Top Skin Shear Strain - Outboard Region

As predicted by finite element analysis, the earliest buckling occurred adjacent to the Kink Rib at around 42% DUL (see Figure 17), with the extent of buckling increasing with load level until the entire panel was extensively buckled. By observing the moiré fringe patterns, the buckling mode showed two and a half wavelengths in the chordwise direction at the ultimate load (see Figures 18 to 21). Compared to the rib load only case, the buckling was delayed due to the initial tension in the bottom skin caused by the wing bending displacements.

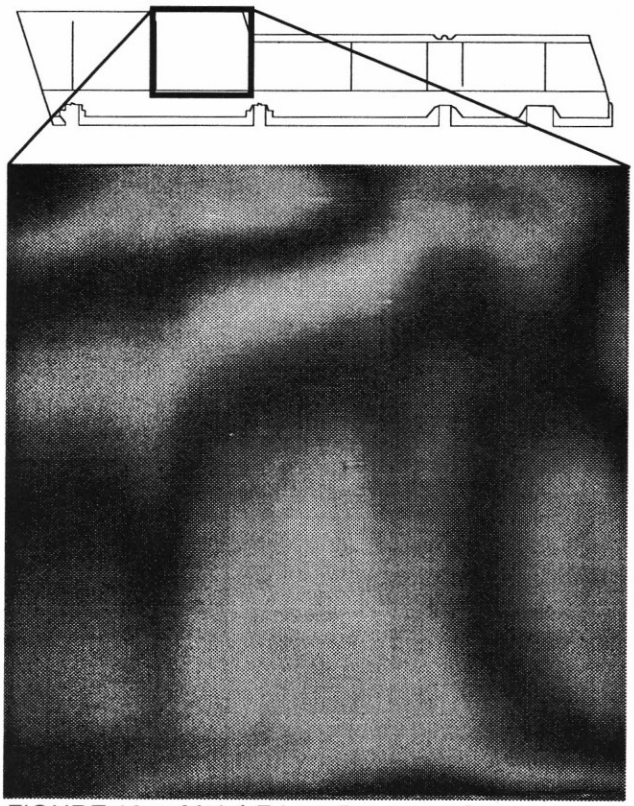

FIGURE 18 - Moiré Fringe Pattern at Outboard End - Zero Rib Load

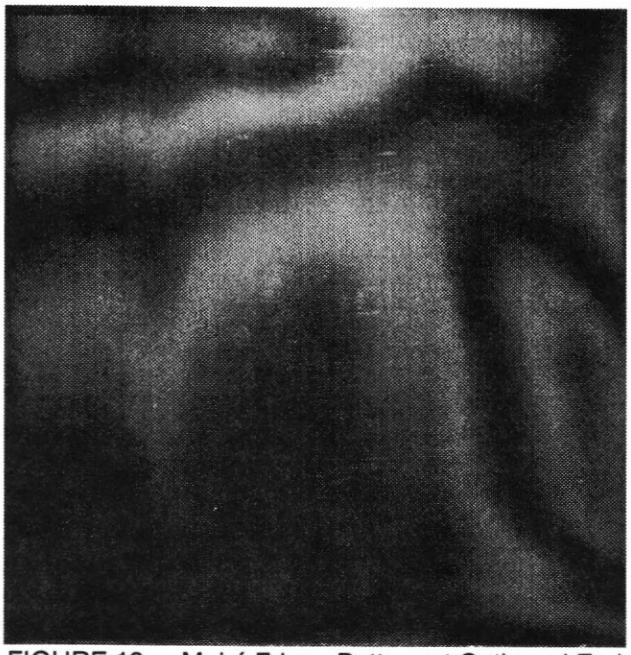

FIGURE 19 - Moiré Fringe Pattern at Outboard End - 40% Rib Load

FIGURE 21 - Moiré Fringe Pattern at Outboard End - 100% Rib Load

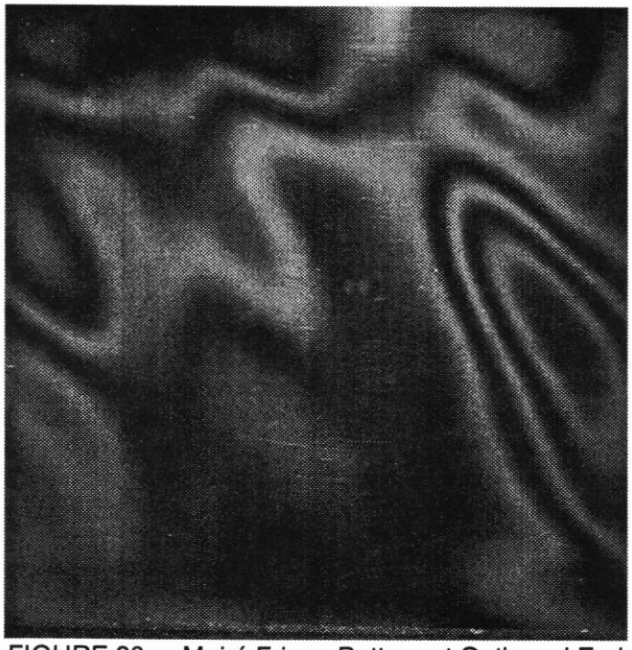

FIGURE 20 - Moiré Fringe Pattern at Outboard End - 70% Rib Load

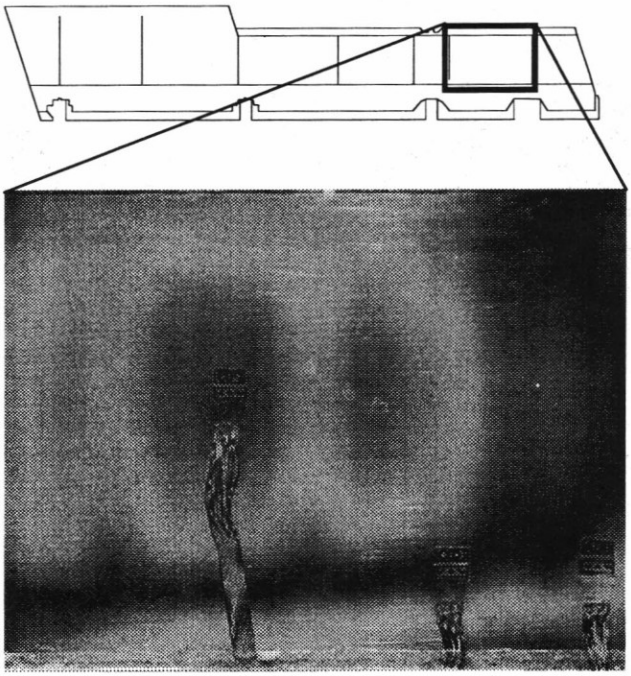

FIGURE 22 - Moiré Fringe Pattern at Inboard End - Zero Rib Load

From the inboard end to the Kink Rib, significant buckling was obvious to the naked eye without the aid of the moiré panel. Each stiffener panel between ribs showed buckling of two half wavelengths inclined to the chord line, which is consistent with shear dominated loading in the skins. This extensive buckling is clearly shown in Figure 27.

On the top skin, compression buckling due to application of the wing bending displacements was clear before applying the rib loads, particularly at the mid-span of the structure.

Between Ribs 2 and 3 on the bottom skins where the highest strains were anticipated, buckling was not

significant until approximately 60% DUL, when fringing in the moiré panel commenced adjacent to Rib 3. With increasing load, further buckling between Ribs 2 and 3 occurred up to 85% DUL (see Figures 22 to 24).

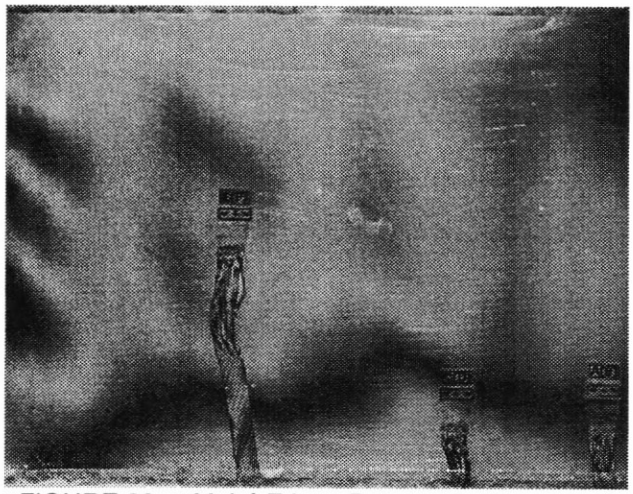

FIGURE 23 - Moiré Fringe Pattern at Inboard End - 75% Rib Load

FIGURE 24 - Moiré Fringe Pattern at Inboard End - 100% Rib Load

Discussion

Although the testing was somewhat simplified in terms of the loading and instrumentation, adequate demonstration of the soundness of the design and the suitability of the analytical technique have been achieved. The fact that no audible emissions from the structure were obtained (apart from the changes in buckling modes) up to the design ultimate load, suggests that the structure would be capable of carrying significantly more load.

Shear strain results from both the FE analysis and the test are shown in Figure 25. The strain measurements were recorded in the stiffened skin close to the Actuator Rib and is considered to be the most critical area. The results show good agreement between analysis and test data.

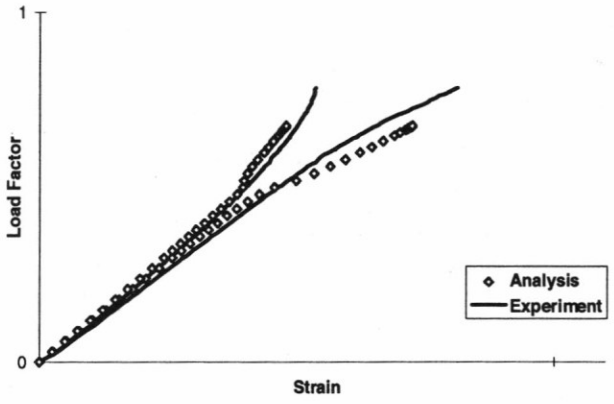

FIGURE 25 - Shear Strain Comparison Between Analysis and Test Results

Figures 26 and 27 present a rendered displacement result from FE analysis, as well as a photograph taken at ultimate load during testing. In Figure 27, moiré fringe screens were applied at bays 2 and 6 from the right of the picture and the buckling patterns are represented by contour lines. Buckling patterns are also clearly visible over the rest of the structure. The comparison between the analytical and experimental buckling modes is also good. The diagonal buckling shape on the stiffened skins is clearly observed in both images.

Conclusions

A number of geometric nonlinear analyses have been successfully conducted, showing MSC/NASTRAN to be an appropriate tool for analysing complex postbuckling structures. Full scale static testing of the control surface has been carried out and the structure survived the ultimate load case without any form of failure. Good agreement in displacement, strain and buckling behaviour between the analytical model and the experimental results was obtained, demonstrating the design method to be suitable. Expected weight savings have been realised with a 34% reduction

being achieved for the control surface aft box structure. This leads to additional weight savings on the total control surface due to the reduction of concentrated weights required for balancing. The manufacturing costs were reduced by 30% [4].

Acknowledgments

The authors would like to gratefully acknowledge the contributions to this work of Shane B. Craddock and Raul A. Martin of Rockwell ASTA Components.

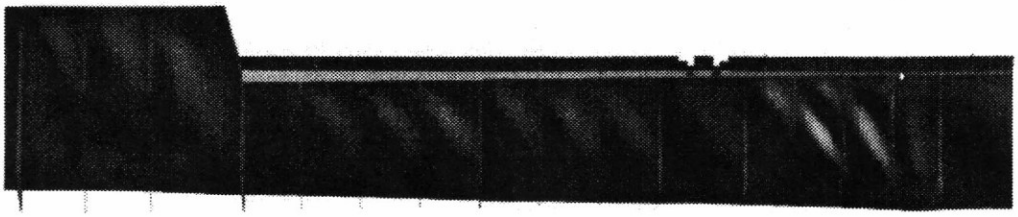

Figure 26 - Finite Element Analysis Result at Design Ultimate Load

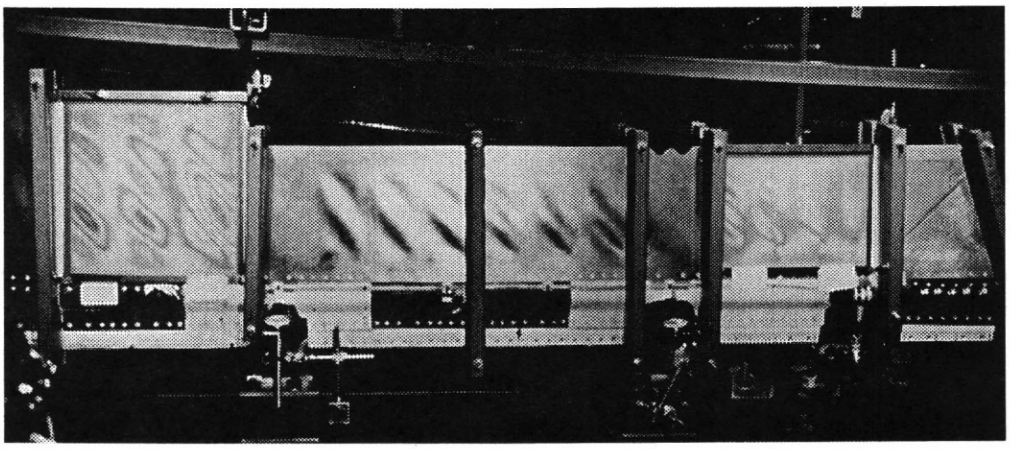

Figure 27 - Test Article at Design Ultimate Load

References

1. Hart-Smith, L.J., Lessons Learned from the DC-10 Carbon-Epoxy Rudder Program. *Douglas Aircraft Paper 7734*, Long Beach, 1986.

2. Hart-Smith, L.J., Innovative Concepts for the Design and Manufacture of Secondary Composite Aircraft Structures, McDonnell Douglas Paper MDC 93K0081, *Proc. Fifth Australian Aeronautical Conference*, Melbourne, Australia, September 13-15, 1993, Vol. 1, 19-49.

3. Trentin, C., Scott, M.L., Alesi H., Postbuckling Behaviour of Blade-Stiffened Fibre Composite Panels, *Proc. Ninth International Conference on Composite Materials*, Madrid, Spain, July 12-16, 1993, Vol. 6, 511-518.

4. Raju, J.A.S., Manufacture of a Co-cured Aileron Aft Box Assembly, *Proc. Second Pacific International Conference on Aerospace Science & Technology - Sixth Australian Aeronautical Conference*, Melbourne, Australia, March 20-23, 1995, Vol. 2, 523-530.

5. Lee, J.M., Ed., MSC/NASTRAN Common Questions and Answers (Second Ed.), MacNeal-Schwendler Corp., Los Angeles, USA, 1993.

6. Lee, S.H., Ed., MSC/NASTRAN Handbook for Nonlinear Analysis (Draft) (Version 67), MacNeal-Schwendler Corp., Los Angeles, USA, 1992.